Drying Technology: An International Journal
Publication details, including instructions for authors and subscription information:
http://www.tandfonline.com/loi/ldrt20

Pore Network Drying Model for Particle Aggregates: Assessment by X-Ray Microtomography

Yujing Wang [a], Abdolreza Kharaghani [a], Thomas Metzger [a] & Evangelos Tsotsas [a]
[a] Thermal Process Engineering, Otto von Guericke University, Magdeburg, Germany
Version of record first published: 14 Nov 2012.

To cite this article: Yujing Wang, Abdolreza Kharaghani, Thomas Metzger & Evangelos Tsotsas (2012): Pore Network Drying Model for Particle Aggregates: Assessment by X-Ray Microtomography, Drying Technology: An International Journal, 30:15, 1800-1809

To link to this article: http://dx.doi.org/10.1080/07373937.2012.713422

Drying Technology, 30: 1800–1809, 2012

ISSN: 0737-3937 print/1532-2300 online
DOI: 10.1080/07373937.2012.713422

Taylor & Francis
Taylor & Francis Group

Pore Network Drying Model for Particle Aggregates: Assessment by X-Ray Microtomography

Yujing Wang, Abdolreza Kharaghani, Thomas Metzger, and Evangelos Tsotsas
Thermal Process Engineering, Otto von Guericke University, Magdeburg, Germany

Convective drying of disordered glass bead packings has been investigated both experimentally and numerically. X-ray microtomography (XMT) and image analysis techniques have been used to determine the three-dimensional spatial distribution of the liquid and solid phases at the pore scale within the wet particle aggregates. The evolution of the liquid distribution in the aggregate has been tracked during the drying process. Particle center coordinates and radii have been extracted from the X-ray images using binarization and segmentation techniques. Based on this geometric data for a real aggregate, a pore network approximation of the pore space has been generated from a Voronoi tessellation about particle centers by designating Voronoi edges as interconnected cylindrical pores with radii computed from the distance between neighboring particles. This three-dimensional irregular pore network takes into account both the geometrical and topological characteristics (pore size distribution and connectivity) of the actual pore space. Drying simulations have been carried out for the pore networks obtained from the XMT and results are presented as phase distributions and moisture profiles. The simulated liquid phase distributions are in qualitative agreement with the experimental result, which indicates that pore network models are suited to describe the drying of dense particle aggregates at the pore scale.

Keywords Convective drying; Liquid distribution; Particle aggregates; Pore-scale simulation; X-ray microtomography

INTRODUCTION

The drying of porous media is a challenge in many industries such as foods, pharmaceuticals, and ceramics. Several modeling attempts have been made to understand the drying characteristics of a porous medium. The traditional continuum approach (Whitaker[1]) considers a continuous porous medium and uses volume-averaged transport equations to describe macroscopic drying behavior. This approach, however, ignores locally dominated phenomena such as gradient-free liquid flow and fractal phase distributions, which are strongly dependent on the microstructure of the capillary porous medium, and can only be described by pore-scale models. The discrete pore network approach represents the void space within a porous medium by a network of interconnected capillaries and uses fundamental physical laws to describe drying phenomena at the pore scale. Since the pioneering work of Fatt,[2] pore network models have become more sophisticated and have been established in the fields of petroleum engineering, hydrology, and environment engineering for better understanding flow behavior in soils and rocks (Berkowitz and Balberg,[3] Blunt[4]). In 1993, Prat[5] combined a pore network model with invasion percolation theory to explore drying behavior in the light of phase patterns and their influence on drying rates. In this approach, drying can be considered as a drainage process during which a wetting phase (liquid) is replaced by a nonwetting phase (gas) as it is evaporating. The classical pore network drying model includes capillary and gravity effects as well as the transport of vapor by diffusion in the gas phase. This proves to be an adequate tool to study the influence of pore structure on drying kinetics (Metzger et al.[6]).

Since then, several research groups have been active in this field to extend the drying model by adding more physical effects and varying geometry and topology of the networks. Major model extensions have been dedicated to viscous effects (Metzger et al.[7]) and film flows (Yiotis et al.[8]). Although classical pore network models use regular grids with a constant coordination number, there is some variety in the geometry of pore throats: the cylinders not only have circular but also regular polygonal cross-sections (Prat[9]; Segura and Toledo[10]). Experimental validation of the network model has been obtained by drying transparent etched networks (Laurindo and Prat[11]). The results have shown good agreement in terms of phase distributions and also pointed out the strong influence of liquid corner films for enhanced mass transfer.

In the above-mentioned extensions and experiments, mainly 2D pore networks have been studied. In order to better describe the behavior of real porous media, Le Bray and Prat[12] first presented results from a 3D simulation with a cubic network of size $51 \times 51 \times 51$. In their analysis, they regard the drying by four periods: initial sharp drop of drying rate before breakthrough (BT); constant rate period (CRP); falling rate period (FRP); and receding front period

Correspondence: Abdolreza Kharaghani, Thermal Process Engineering, Otto von Guericke University, P.O. Box 4120, 39016 Magdeburg, Germany; E-mail: abdolreza.kharaghani@ovgu.de

(RFP). All these periods are related to the liquid phase distribution. Later on, Yiotis et al.[13] confirmed these by simulations on pore networks of size $80 \times 80 \times 80$; they also included the effect of gravity. Kharaghani et al.[14] proposed a 3D network model, which was interpreted as the void space of a regular aggregate of monodisperse spherical particles; this model included liquid-solid interaction due to capillary forces by discrete element method (DEM), and the study was focused on mechanical effects (cracks, shrinkage) during drying.

All these models were based on regular lattices, and only pore (throat) size was a random variable. However, real porous media, which are attempted to be modeled, have a more complicated structure. To overcome this limitation and to provide a more realistic description, various representations of pore network models have been used in the field of petroleum and environment engineering. The main distinction is the specific method used to construct the network. The parameters describing geometry of a network mainly decide which method is appropriate for network generation. Relevant parameters are, for instance, spatial dimension (2D or 3D), grid arrangement (regular or irregular), and coordination number (network connectivity). In order to include irregularity and randomness of grid arrangement into pore networks, Voronoi tessellation is a very common method (Thompson and Fogler,[15] Jerauld et al.,[16] and Blunt and King[17]). Recently, Kharaghani[18] has utilized this method to generate a 3D irregular network to map the void space of a random packing of mono-sized particles generated by DEM and then applied the established drying algorithm. Figure 1 gives an example of such a network during drying, illustrating that the randomness of node locations and connectivity can more accurately be captured.

Besides the theoretical studies, many researchers have used 3D image techniques such as magnetic resonance imaging (MRI) and X-ray microtomography (XMT) to "visualize" the liquid evolution within porous materials during drying. Pel and co-workers (Pel and Kopinga,[19] Valckenborg et al.[20]) have investigated moisture profiles and water distribution during drying of porous building materials (brick and mortar samples) by using MRI. More recently, Faure and Coussot[21] have also used MRI to study drying behavior of model soils, presenting the time evolution of the water saturation distribution inside the soil sample.

X-ray microtomography (XMT), as used in this study, is able to determine the inner structure of a porous sample with high resolution. Nowadays, this technique is not limited to medical applications, but it is widely and successfully applied in scientific or industrial fields such as hydrogeology (Wildenschild et al.[22]), powder technology (Farber et al.[23]), and pharmaceutics (Fu et al.[24]). Since the development of microfocus and CCD camera allowed the image to achieve high resolution (around 1 μm), this technique is extensively applied in materials science, also related to drying, e.g., to assess the deformation of xerogels during drying (Léonard et al.[25]). Kohout et al.[26] have tracked the evolution of moisture profile during drying of an alumina particle packing. A general literature review concerning recent advances in X-ray tomography has been given by Stock,[27] and explicitly drying-related applications of XMT have been summarized by Léonard et al.[28]

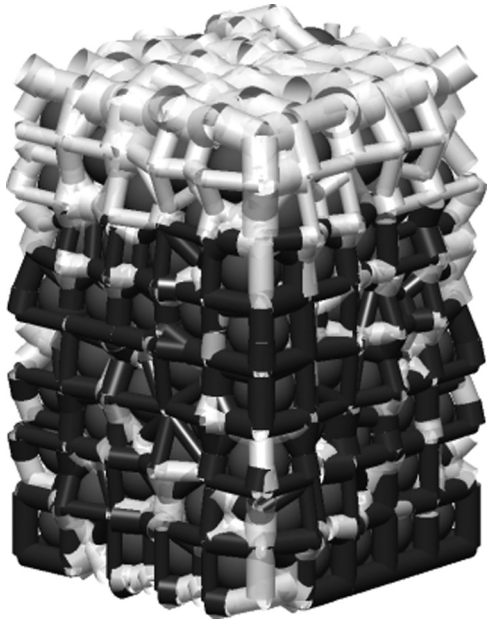

FIG. 1. The simulated liquid distribution for a 3D irregular pore network model (Kharaghani[18]).

The principle of X-ray microtomography is that an X-ray beam is attenuated as it passes through the material. According to Beer-Lambert's law, an X-ray beam of intensity I_0 passing through a simple material of thickness d to yields a transmitted beam of intensity

$$I = I_0 e^{-\mu d} \tag{1}$$

The attenuation coefficient μ depends on density ρ and atomic number Z of the material and on beam energy E

$$\mu = \rho\left(a + \frac{bZ^{3.8}}{E^{3.2}}\right) \tag{2}$$

where a is a parameter which slightly depends on the energy E and b is a constant (Vinegar and Wellington[29]). If the material is not uniform, e.g., consists of different phases, then the attenuation is obtained by integrating along the transmission path

$$\int \mu(s)ds = \ln\left(\frac{I}{I_0}\right) = P \tag{3}$$

where $\mu(s)$ is the linear attenuation coefficient at position s. The projection signal P contains information from the whole transmission path; and in order to extract local information on $\mu(s)$, multiple scans (projections) are obtained from many angles (by rotating the sample from 0° to 360°) and used for reconstruction by a filtered backprojection algorithm (Kak and Slaney[30]). Each voxel in the reconstructed 3D image has a gray value corresponding to the local attenuation coefficient. According to this principle, the inner structure of the porous material can be obtained and different phases can be distinguished if they have different attenuation characteristics.

This paper reports on an experiment with a particle packing that has been dried in an X-ray micro-tomographic device. The reconstructed 3D images have been segmented into the three phases (solid, liquid, and gas) by thresholding; these phase images are presented to visualize the liquid-gas interface in the individual pores and to illustrate the evolution of liquid distributions as drying proceeds. Furthermore, particle center coordinates and radii extracted from these images are utilized to generate a 3D irregular pore network by use of Voronoi tessellation and strategies for boundary cell elimination and merging of close nodes. A network drying algorithm is applied to this matched pore network and results are given as phase distributions and moisture profiles. Such efforts are taken to explore how well drying behavior of particle aggregates can be approximated by the pore network approach. By this technique, the pore network model can be assessed at the pore level.

X-RAY MICROTOMOGRAPHY OF PARTICLE AGGREGATES DURING DRYING

Experimental Set-Up for Drying

The drying of a glass bead packing filled with distilled water was investigated experimentally. The glass beads (SiLibeadsvfrom Sigmund Linder GmbH, Germany) with a mean diameter of 0.8 mm were carefully selected for high sphericity and uniformity in size. The container had a cylindrical shape with an inner diameter of 8 mm to optimally use the imaging space, and it was made from plastic (PMMA), because this material is relatively transparent to X-rays compared to the water-glass system. The glass beads were carefully packed into the container filled with water to form a water-saturated packed bed of about 8 mm height. The liquid-gas interface was touching the surface of the topmost glass beads.

A laboratory X-ray microtomograph (CT-ALPHA-160 by ProCon X-Ray GmbH, Germany) was used to scan the glass bead packing during drying. This device is equipped with a microfocus X-ray source and has a detector size of 2300×2300 pixels. As illustrated in Fig. 2, the sample was mounted on a rotating holder and dried naturally without control of temperature or air condition. The

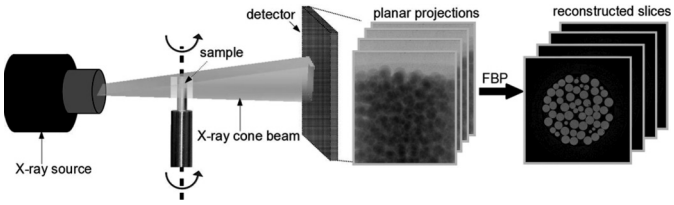

FIG. 2. Scheme of the cone beam microtomography setup and image reconstruction procedure.

X-ray cone beam was generated at 90 kV and 160 μA. By adjusting the distances between the source, sample, and detector, the spatial resolution was set to approximately 5 μm. One scan takes around two hours to run: 12-bit transmission images are collected from 800 different angles (step size 0.45°) for subsequent 3D tomographic reconstruction. The measurement and reconstruction software Volex (ITWM[31]) (developed by Fraunhofer Institute for Integrated Circuits IIS Erlangen, Germany) was used to obtain a three-dimensional gray level array.

Since the drying was very slow, drying rate was expected to have no influence on phase distributions [viscous and thermal effects being negligible (Huinink et al.[32])]. At intervals of 30 minutes, the container was gently sealed by sticky tape to interrupt the drying process and to perform an X-ray scan. The sample stayed in the X-ray equipment during the whole drying and scanning to avoid particle displacement.

Image Processing and Data Analysis

To improve the image quality and to allow for geometric analysis, several image processing steps have been performed by the MAVI software (ITWM[33]) (developed by Fraunhofer Institute for Technical and Industrial Mathematics, Kaiserslautern, Germany), as illustrated in Fig. 3. First, the unwanted regions (e.g., container walls) were cropped from the original full resolution images (see Fig. 2 for reconstructed slices) and down sampling by a factor of 4 was used to reduce the memory requirements while retaining sufficient resolution. This resulted in an $838 \times 839 \times 620$ array of $(19.7\ \mu m)^3$, which is sufficient to describe our sample (around 40 voxels per particle diameter). Then, a median filter was applied to smoothen the edges and to reduce the noise. Since the investigation of the spatial distribution and evolution of the liquid phase during drying is the main purpose of this study, assigning a single phase (solid, liquid, or gas) to each voxel is a crucial image analysis step. Therefore, the gray-scale images have been segmented into the individual phases by use of the histogram of gray levels, which represents the solid, liquid, and gas phases as three peaks separated by two valleys, where the respective threshold values were chosen. The segmentation process replaces the phase of interest by a gray level of 255 (white) and the values of all other voxels by 0 (black); then the gray-scale

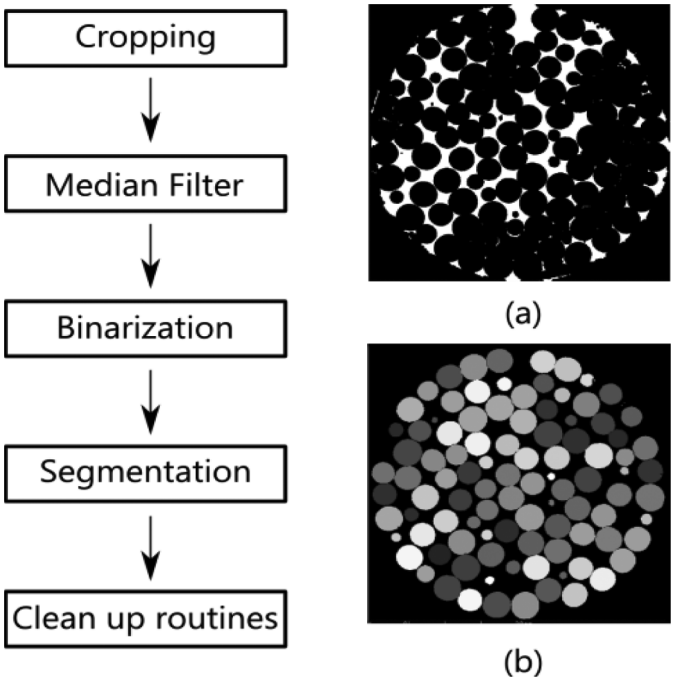

FIG. 3. Image processing steps of X-ray images with (a) binarized image of liquid phase and (b) segmented particles after treatment with preflood watershed algorithm.

image is binarized (Fig. 3a shows a liquid-phase binary image). Here, it should be mentioned that the same threshold values could be used for the different fluid saturation states occurring during drying. A clean-up routine applied to the solid phase was used to remove gas bubbles in the glass beads. In order to obtain the center coordinates and radii of the individual solid particles, the binarized solid-phase images were segmented by using the pre-flood watershed algorithm (ITWM[33]) (Fig. 3b). Another clean-up routine was applied to the liquid phase such that the voxels belonging to both liquid and solid phases were assigned to be only the solid. Thus, the thin artificial liquid layer on the solid surface was removed, which also appears in the dry sample image due to the use of a single threshold value for the gradual transition of the attenuation coefficient in solid-fluid voxels. Three-dimensional visualizations of the wet particle packing are presented in Fig. 4. They show the phase distributions within the sample; the solid, liquid, and gas phases are easily distinguished and the pore structure of the packing is well observed. Finally, the segmented images, particle center coordinates, and radii of separated particles were used to generate an irregular pore network in MATLAB, as described in the next section.

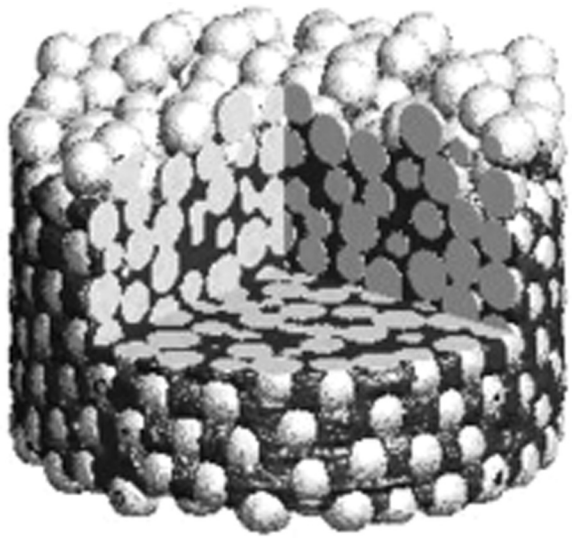

FIG. 4. 3D visualization of a partially saturated particle aggregate at saturation S = 60%.

METHODS

Pore Network Generation Algorithm

The Voronoi tessellation has been used to approximate the void space of the particle aggregate obtained from the tomography measurement by a three-dimensional pore network. The Voronoi algorithm uses particle center coordinates to segment the pore space into non-overlapping polyhedral cells (Voronoi[34]). The pore network geometry is described by nodes corresponding to vertices in the Voronoi tessellation and by cylindrical pores, with axes corresponding to edges in the Voronoi tessellation. The radius of each pore is calculated from the distance of the cylinder axis to the neighboring particle surfaces. The pore network thus obtained from a monodisperse particle packing has a realistic variability in pore size and orientation.

Figure 5 shows how a bounded network can be generated from a given particle distribution with little overlap between pores. For a given distribution of generator particles (Fig. 5a), the Voronoi tessellation contains unbounded cells (Fig. 5b) which are removed (Fig. 5c). A bounded network is then established by designating the remaining Voronoi edges as pores (Fig. 5d) – for further details, see Kharaghani.[35]

The following algorithm was employed to construct a pore network approximation for the void space of real particle aggregates:

1. The center coordinates and radii of the particles were extracted from the X-ray images (Fig. 6a).
2. Particles adjacent to the side and bottom inner wall of the cylindrical container are identified and mirrored to generate two artificial layers of particles outside the main aggregate (Fig. 6b).
3. In order to generate a boundary layer above the particle aggregate responsible for lateral vapor diffusion in the drying simulations (Metzger et al.[6]), two regularly

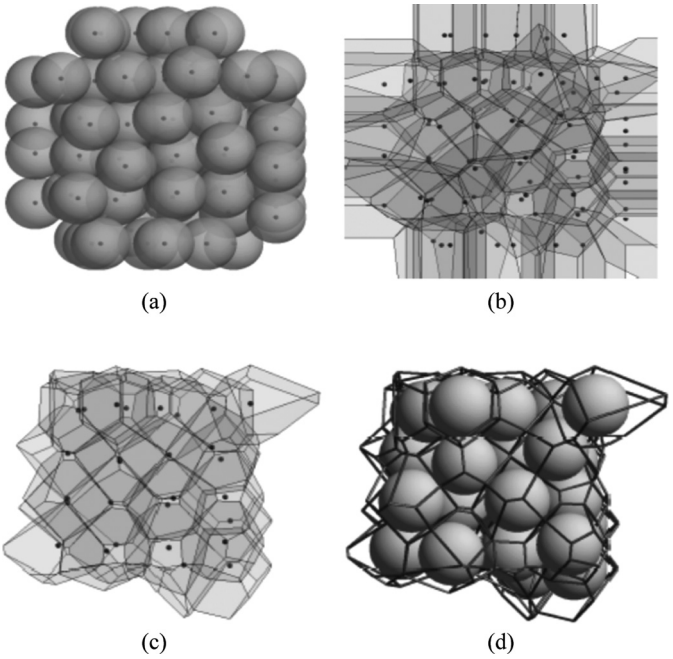

FIG. 5. Network generation strategy: (a) generators, (b), (c) Voronoi tessellation before and after elimination, and (d) resulting pore networks (Kharaghani[18]).

packed layers of particles are added on top. The final aggregate containing both the primary particles and the new additional layers are shown in Figure 6b.

4. The particle center coordinates of the final aggregate are considered as generators for a 3D Voronoi tessellation. Unbounded cells and generator particles are removed, such that only bounded cells remain. The Voronoi edges are considered as cylindrical pores and vertices as nodes.

The Voronoi tessellation of a particle packing may contain very short edges, which leads to a relatively large overlap between pores. Therefore, a merging algorithm (illustrated by an example in Fig. 7) was developed to eliminate edges which are shorter than a predefined threshold:

1. The length of each edge (i,j), $L_{ij} = \| \mathbf{v}_j - \mathbf{v}_i \|$ is computed from the corresponding vertex coordinates, $\mathbf{v}_i$ and $\mathbf{v}_j$.

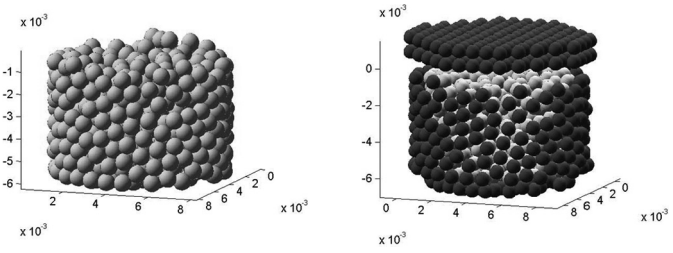

FIG. 6. (a) Particle packing with (b) layers of virtual particles (in dark gray) for Voronoi tessellation.

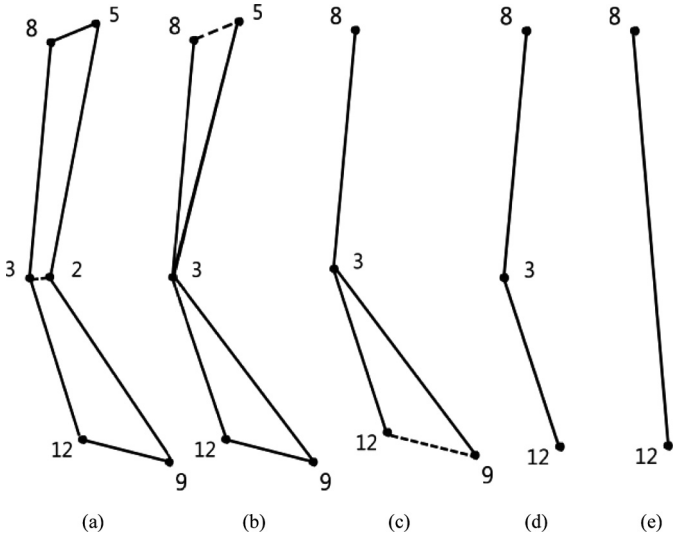

FIG. 7. Merging steps: (a) collect short edges (dashed lines) connected with node $\mathbf{v}_3$, (b) elimination of smallest edge and merging of node $\mathbf{v}_2$ with node $\mathbf{v}_3$. Case of middle node: (c) after merging $L_{3,9}$ and $L_{9,12}$ middle node $\mathbf{v}_3$ is aroused (d) and removed (e).

3. An edge which is shorter than a given threshold, such as (2, 3) in Fig. 7a, is selected and removed by merging its two nodes. The node i is removed and all edges connecting to i are reconnected to node j.
4. Edge lengths are updated for the new network topology. Then the algorithm restarts from step 1 for the next edge until the shortest edge in the network is longer than the threshold.
5. Following steps 1–3 may cause so-called "middle-node" cases. As shown in Figs. 7a–7d, merging operations reduce the coordination number of node 3 to 2. Such nodes are removed and their neighbors connected directly (Fig. 7e).

The network connectivity is expressed by the coordination number distribution (i.e., the number of pores emanating from each node), which depends on the properties of the porous medium and on the technique utilized to construct a network. Jerauld and Salter[36] concluded that coordination numbers in the range of 4 to 8 are realistic for three-dimensional porous media. Histograms of the coordination number distribution for pore networks extracted from a particle aggregate (Fig. 6a) before and after elimination of pores shorter than 20% of the particle radius are shown in Fig. 8. Note that the most frequent coordination number is 4, and that the node merging algorithm significantly increases the dispersion of the coordination number to the range of 3 to 8. This implies that after merging the network represents the complexity of a real aggregate more realistically. It should be emphasized that the threshold value is a key parameter in the node merging strategy. If the threshold value is chosen too large,

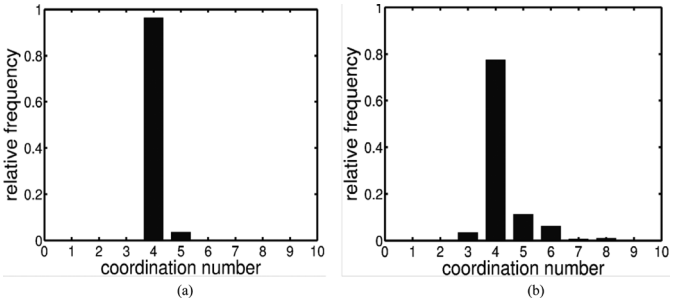

FIG. 8. Relative frequency of coordination number for networks: (a) without elimination of short pores and (b) pore lengths shorter than 20% of particle radius are merged.

for example, then the algorithm will remove many pores and increase the mean coordination number to an unreasonably large value; the network may thus significantly change its shape and lead to an unrealistic representation of the void space, where pores may pass through particles, for example. Related pore length distributions are shown in Fig. 9. It can be seen that many short edges are generated by the Voronoi algorithm and that the pore length distribution shifts to slightly large values upon applying the node merging strategy. A particle aggregate, together with its complementary pore network, after applying a merging threshold of 20% of the particle radius, is shown in Fig. 10.

Pore Network Drying Algorithm

An existing isothermal pore network drying model, which neglects viscosity, gravity, Kelvin and Knudsen effects, is employed to simulate the drying with a 3D pore network generated from image analysis of a real particle packing, as described above. Film effects are not relevant for the chosen cylindrical geometry of pores. The particle aggregate is exposed to convective drying at the top surface; initially, it is completely saturated with water. Mass transfer occurs by vapor diffusion in the gas-filled region and by capillary flow in the liquid-filled part of the pore space. A

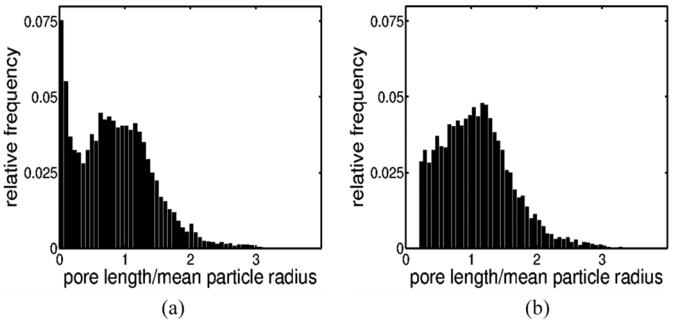

FIG. 9. Pore length distributions for networks: (a) without elimination of short pores and (b) pore lengths shorter than threshold value of 20% of particle radius are merged.

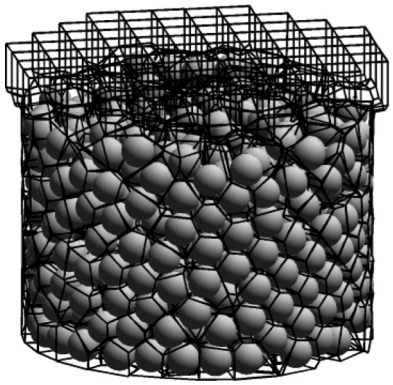

FIG. 10. A 3D irregular pore network generated by Voronoi tessellation, cell elimination, and node-merging (cylindrical pores are presented by lines).

detailed description of the drying algorithm used in this simulation is given in Metzger et al.[6]

RESULTS AND DISCUSSIONS

Experimental Drying Results

The microstructure geometry of solid phase and the evolution of liquid phase distributions during drying are shown as reconstructed horizontal and vertical cross-sections in Fig. 11. The major physical effect of capillary flow from large pores into small pores can be seen by comparing images horizontally (left to right): large pores dry out first, while the small pores stay saturated with liquid. The gas phase invades the depth of the aggregate, and fractal

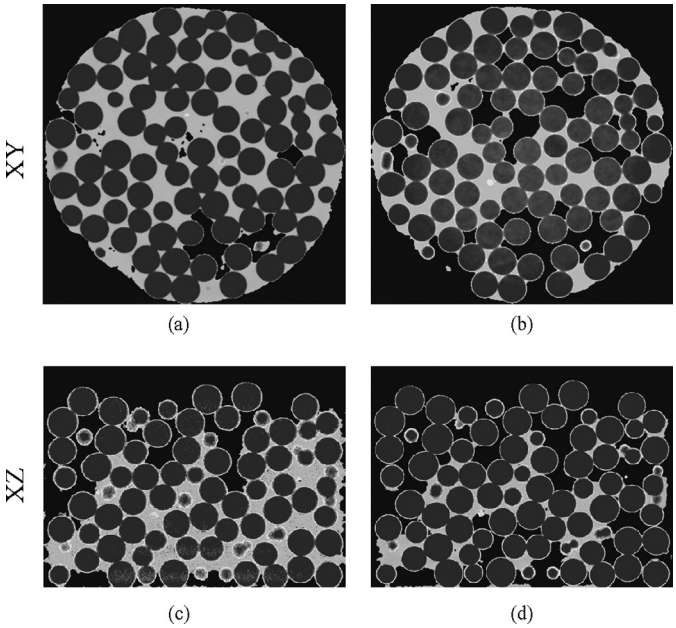

FIG. 11. Evolution of liquid distribution during drying at saturation (a), (c) S = 35% and (b), (d) S = 20% (dark gray: solid, light gray: water, black: air).

patterns of drying front presented with emerging liquid clusters of various sizes are recognized in the vertical cross-sections (Figs. 11c and 11d).

According to the slice images, total saturation is calculated by

$$S(t) = \frac{V_\ell(t)}{V_c - V_s} \tag{4}$$

where V_c is the volume of the container, and V_ℓ and V_s denote liquid and solid volumes, respectively. These are calculated by voxel size times voxel number of each phase. Within the limits of experimental set-up concerning constant drying conditions and drying time determination, a first drying period with a constant drying rate is observed in Fig. 12.

Three-dimensional rendering images showing the evolution of liquid distributions for overall saturations of 35%, 30%, and 20% are given in Fig. 13 (only the center of the sample is depicted). On the one hand, it is noticed that near the open side small liquid clusters are separated from the main liquid cluster, which on the other hand is still spanning the main region of the packing until the last experimental recording (S = 20%). These phenomena are typical for an invasion percolation process.

The pertinent question now is whether such behavior found in the experiment can also be described by a pore network approximation of pore space and the related drying algorithm. To address this, a pore network drying simulation has been performed.

Simulation Results and Discussion

The simulation results obtained by the non-viscous drying algorithm are presented in Fig. 14. At the very beginning of drying, the partially saturated pores are all

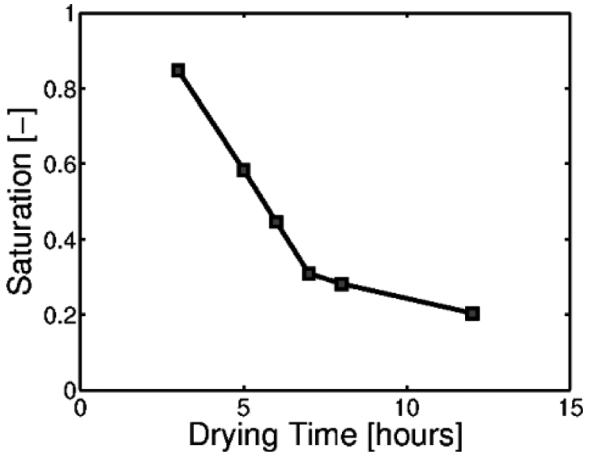

FIG. 12. Overall saturation as a function of time for the particle aggregate shown in Fig. 10.

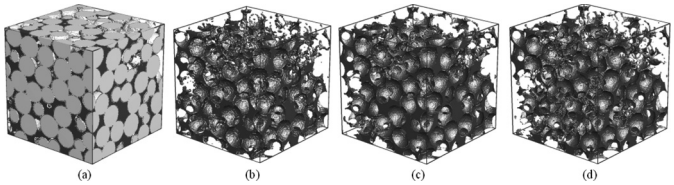

FIG. 13. Evolution of spatial liquid phase distributions during drying at saturation S = 35% (a) with solid and liquid phase and (b) only liquid phase; (c) S = 30% and (d) S = 20%.

located at the aggregate surface and the main liquid cluster is connected to the opening surface (Fig. 14a). Breakthrough is happening when gas penetrates into the depth of the network along the wall where pores have larger radii (Fig. 14b). The main liquid cluster is still connected to the network surface for a while, pumping the liquid to the surface from inner pores by capillary flow, and the gas cluster grows within the aggregate (Fig. 14c). In the progress of drying, disconnected clusters form and only the liquid clusters near the open side can evaporate and contribute to the drying rate while the gas phase around the clusters deep in the aggregate is saturated with vapor. Therefore, all surface pores dry out due to the disconnection of liquid and drying front recedes into the aggregates (Fig. 14d), which is identified as the receding front period (RFP) by Le Bray and Prat.[13]

A quantitative comparison between experimental and simulation results made by evolution of the averaged slice saturation profiles along the vertical direction is shown in Fig. 15 for experimental data (a) and simulation results (b).

Experimental averaged saturation of horizontal planes at time t with given vertical coordinate z is calculated by

$$S(z,t) = \frac{A_\ell(z,t)}{A_c - A_s(z)} \tag{5}$$

where A_ℓ and A_s denote, respectively, the liquid and solid phase area and are calculated from the size and number of pixels associated to each phase. A_c is the cross-section area of the cylindrical container.

Saturation profiles for the pore network simulation have been obtained by discretizing the vertical direction of the

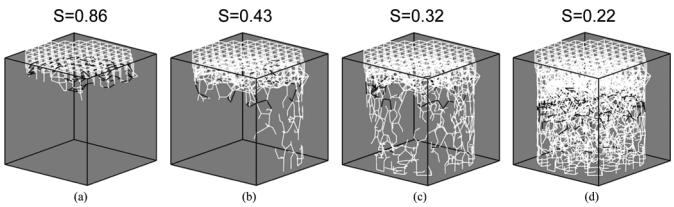

FIG. 14. Theoretical evolution of liquid distribution in pore network during drying. Top face is open to dry; only empty pores (white lines) and partially saturated pores (black lines) are plotted.

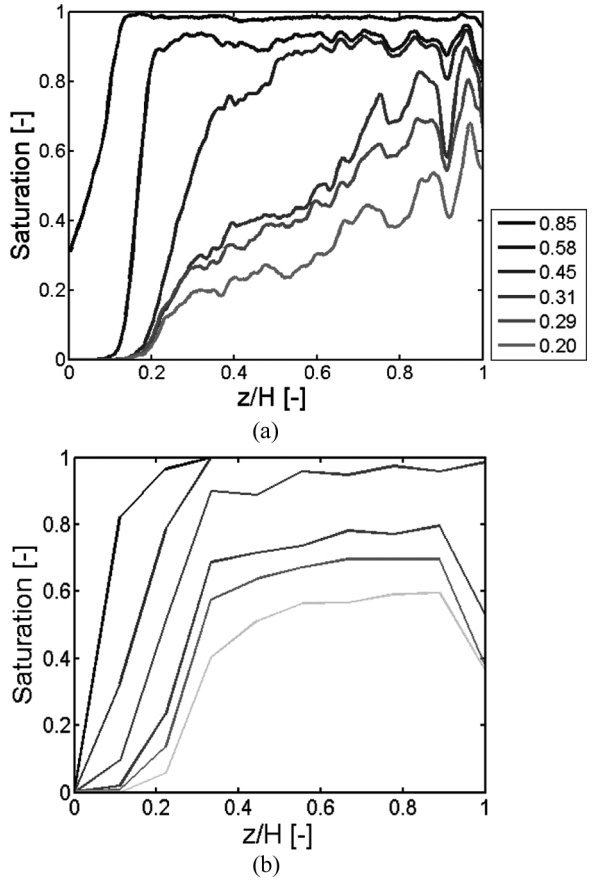

FIG. 15. Evolution of liquid profiles in z direction (horizontally averaged saturation) during drying: (a) experimental data, (b) pore network simulation results. (H represents the overall height of the packing.)

network and computing the average saturation for pores associated to each such interval.

In both experiment and simulation, the averaged slice-saturation profiles have been plotted at the same total saturations. Relatively good agreement can be found in the first drying period. After the first drying period, the experimental saturation profiles show a significant gradient (Fig. 15a), whereas the simulated profiles may be considered as gradient-free. In the experiment, the saturation near the sample surface (at position $z/H = 0.2$) stays almost constant while the main packing is losing liquid in both experiment and simulation; the sample surface remains partially wet down to an overall saturation of around 0.2. This is because the drying front is pinned in smaller pores for a significant period, while the water is continually removed from the depth of the packing by capillary pumping to the surface, where it evaporates.

The discrepancy between experimental and simulation results may have several reasons, which will have to be investigated in more detailed future work:

1. The pore spaces, which are used to describe and compare liquid saturations at a local and a global scale, are not identical. The cylindrical pores in the simulation do, on the one hand, not account for the wedge-shaped pore fractions near the inter-particle contacts; on the other hand, they do have some overlap at the nodal points of the network. Therefore, the description of pore space is approximate and the influence on saturation computation is not clear.
2. The approximate nature of the network model goes further: annular liquid films around the particle-particle contact points are not accounted for in the mass transfer description. In reality, they can maintain long-distance liquid connections between liquid pores that would otherwise be separated; this has been nicely proven by Scheel et al.[37] The effect of this neglected phenomenon on the emptying sequence of pores is not evident.
3. Finally, the network model neglects gravity, which is well known to have a stabilizing effect on the drying front[5] and might (partly) explain the gradient in experimental saturation profiles.

Despite the differences between experimental and simulated drying behavior, the major characteristic is captured by the network model, namely the capillary effect, which—at the micro scale—leads to a one-by-one emptying of pores with decreasing size and—at the macro scale—results in liquid removal from the depth of the packing and a pronounced first drying period.

CONCLUSIONS

In this work, X-ray microtomography and image analysis have been utilized to extract the microstructure of a particle packing for generating a 3D irregular pore network and to investigate the evolution of liquid distribution during drying at the pore scale. The reconstructed solid phase images were segmented into individual particles and used to extract center coordinates and radii of glass beads in a cylindrical packing. Based on this geometric data, a first irregular pore network with interconnected cylindrical pores representing the void space of the aggregate was constructed by Voronoi tessellation. The pore lengths are the lengths of the Voronoi edges and the pore radii have been computed from the distance between neighboring particles. Performing a cell elimination and node-merging algorithm, the structural features of the pore space in the real aggregate, such as spatial correlations in the distribution of pore length and coordination number of the network, are captured more accurately.

The pore network drying algorithm from literature has been applied to the new irregular networks, and simulation results have been shown as liquid phase distributions. The evolution of liquid distribution profiles of experiment and simulation provide an opportunity to investigate the dynamic processes such as capillary phenomena, drying front widening, and film effects in complex porous microstructures during drying. Major drying phenomena caused

by capillary effects can already by captured by the basic network model, but the assessment of the pore network model is still at its beginning. In a next step, gravity will be included to see whether the gradient in experimental saturation profiles can be described.

A more advanced model extension should address the film effects. In the bead packing, their description seems to necessitate a different approach than used for the corner films in etched micromodels.[8,9] In the particle packing, films exist at particle contacts as annular objects, which cannot be described as part of the (cylindrical) pores of the network, but form independent entities. Besides their ability to link separate liquid-pore clusters, they may also exist as isolated binary liquid bridges. (For a nice illustration, see the work of Scheel et al.[37])

In our approach, the particle packing is seen as a better representative of real porous media than etched micro models. Indeed, many real porous materials are built from primary particles by processes such as gelation, sintering, or agglomeration.

For better comparison between measured and simulated drying behavior, the experimental set-up shall also be improved: the micro tomographic device will host a supply line for preheated dry air and a sensor for recording temperature to have controlled drying conditions. Furthermore, data processing will be enhanced: the cylindrical pores of the network model will be identified as sets of experimental voxels. Then, the filling state of these theoretical pores can be evaluated from the experiment and directly compared to the pore network simulation.

Improved experiments and data processing are expected to contribute significantly to the improvement of the existing pore network drying models through incorporating pore-level effects such as film flows.

NOMENCLATURE

A	area m^2
E	beam energy eV
H	height of packing m
I	intensity $W \cdot m^{-2}$
L	edge length m
P	projection -
S	saturation -
V	volume m^3
Z	atomic number -
d	thickness m
t	time s
v	vertex coordinates -
z	distance to network surface m

Greek letters

μ	linear attenuation coefficient -
ρ	density $kg\,m^{-3}$

Subscripts and superscripts

g	gas
c	container
i, ij	indices of node, pore
l	liquid (water)
s	solid

ACKNOWLEDGMENTS

This work was financed by the German Research Foundation (DFG) in the frame of Graduate School GRK 1554 "Micro-Macro-Interaction in Structured Media and Particulate Systems." The X-ray tomography device used in this study was financed by the EFRD (European Fund for Regional Development) in project no. 121108002.

REFERENCES

1. Whitaker, S. Simultaneous heat, mass and momentum transfer in porous media: A theory of drying. *Advances in Heat Transfer* **1977**, *13*, 119–203.
2. Fatt, I. The network model of porous media I: Capillary pressure characteristics. *AIME Petroleum Transactions* **1965**, *207*, 144–159.
3. Berkowitz, B.; Balberg, I. Percolation theory and its application to groundwater hydrology. *Water Resources Research* **1993**, *29*(4), 775–794.
4. Blunt, M.J. Flow in porous media—pore-network models and multiphase flow. *Current Opinion in Colloid and Interface Science* **2001**, *6*, 197–207.
5. Prat, M. Percolation model of drying under isothermal conditions in porous media. *International Journal of Multiphase Flow* **1993**, *19*, 691–704.
6. Metzger, T.; Irawan, A.; Tsotsas, E. Influence of pore structure on drying kinetics: A pore network study. *AIChE Journal* **2007**, *53*, 3029–3041.
7. Metzger, T.; Irawan, A.; Tsotsas, E. Isothermal drying of pore networks: Influence of friction for different pore structures. *Drying Technology* **2007**, *25*, 49–57.
8. Yiotis, A.G.; Boudouvis, A.G.; Stubos, A.K.; Tsimpanogiannis, I.N.; Yortsos, Y.C. Effect of liquid films on the isothermal drying of porous media. *Physical Review E* **2003**, *68*, 037303.
9. Prat, M. On the influence of pore shape, contact angle and film flows on drying of capillary porous media. *International Journal of Heat and Mass Transfer* **2007**, *86*, 153–164.
10. Segura, L.A.; Toledo, P.G. Pore-level modelling of isothermal drying of pore networks: Effects of gravity and pore shape and size distributions on saturation and transport parameters. *Chemical Engineering Journal* **2005**, *111*, 237–252.
11. Laurindo, J.B.; Prat, M. Numerical and experimental network study of evaporation in capillary porous media: Drying rates. *Chemical Engineering Science* **1998**, *53*, 2257–2269.
12. Le Bray, Y.; Prat, M. Three-dimensional pore network simulation of drying in capillary porous media. *International Journal of Heat and Mass Transfer* **1999**, *42*, 4207–4224.
13. Yiotis, A.G.; Tsimpanogiannis, I.N.; Stubos, A.K.; Yortsos, Y.C. Pore-network study of the characteristic periods in the drying of porous materials. *Journal of Colloid Interface Science* **2006**, *297*, 738–748.
14. Kharaghani, A.; Metzger, T.; Tsotsas, E. A proposal for discrete modeling of mechanical effects during drying, combining pore networks with DEM. *AIChE Journal* **2011**, *57*, 872–885.
15. Thompson, K.E.; Fogler, H.S. Modeling flow in disordered packed beds from pore-scale fluid mechanics. *Fluid Mechanics and Transport Phenomena* **1997**, *43*, 1377–1389.

16. Jerauld, G.R.; Scriven, L.E.; Davis, H.T. Percolation and conduction on the 3D Voronoi and regular networks: A second case study in topological disorder. *Journal of Physics C* **1984**, *17*, 3429–3439.
17. Blunt, M.; King, P. Relative permeability from two- and three-dimensional pore-scale modelling. *Transport Porous Media* **2001**, *6*, 407–433.
18. Kharaghani, A. Irregular pore networks and mechanical effects during drying of porous media, PhD thesis, Otto-von-Guericke-Universität, Magdeburg, Germany, 2010.
19. Pel, L.; Kopinga, K. Moisture transport in porous building materials. *HERON* **1996**, *41*, 95–105.
20. Valckenborg, R.M.E.; Pel, L.; Hazrati, K.; Kopinga, K.; Marchand, J. Pore water distribution in mortar during drying as determined by NMR. *Materials and Structures* **2001**, *34*, 599–604.
21. Faure, P.; Coussot, P. Drying of a model soil. *Physical Review E* **2010**, *82*, 036303.
22. Wildenschild, D.; Vaz, C.M.P.; Rivers, M.L.; Rikard, D.; Christensen, B.S.B. Using X-ray computed tomography in hydrology: Systems, resolutions, and limitations. *Journal of Hydrology* **2002**, *267*, 285–297.
23. Farber, L.; Tardos, G.; Michaels, N.J. Use of X-ray tomography to study the porosity and morphology of granules. *Powder Technology* **2003**, *132*, 57–63.
24. Fu, X.; Dutt, M.; Bentham, A.C.; Hancock, B.C.; Cameron, R.E.; Eliott, J.A. Investigation of particle packing in model pharmaceutical powders using X-ray microtomography and discrete element method. *Powder Technology* **2006**, *167*, 134–140.
25. Léonard, A.; Job, N.; Blacher, S.; Pirard, J.P. Crine, M.; Jomaa, W. Suitability of convective air drying for the production of porous resorcinol-fomaldehyde and carbon xerogels. *Carbon* **2005**, *43*, 1808–1811.
26. Kohout, M.; Grof, Z.; Stepanek, F. Pore-scale modelling and tomographic visualisation of drying in granular media. *Journal of Colloid and Interface Science* **2006**, *299*, 342–351.
27. Stock, S.R. Recent advances in X-ray microtomography applied to materials. *International Materials Reviews* **2008**, *53*, 129–181.
28. Léonard, A.; Crine, M.; Stepanek, F. Chapter 4 Use of X-ray tomography for drying-related applications. In *Modern Drying Technology: Volume 2: Experimental Technique*; Tsotsas, E.; Mujumbar, A.S., Eds.; Wiley-VCH Verlag GmbH & Co. KGaA: Weinheim, 2008; 143–186.
29. Vinegar, H.J.; Wellington, S.L. Tomographic imaging of three-phase flow experiments. *Review of Scientific Instruments* **1987**, *58*(1), 96–107.
30. Kak, A.C.; Slaney, M. *Principles of Computerized Tomographic Imaging*; Society of Industrial and Applied Mathematics: Philadelphia, PA, 2001.
31. Fraunhofer ITWM. *Volex – Manual 3D-Computertomography*, 2009.
32. Huinink, H.P.; Pel, L., Michels, M.A.J.; Prat, M. Drying processes in the presence of temperature gradients, pore scale modeling. *The European Physical Journal E: Soft Matter and Biological Physics* **2002**, *9*, 487–498.
33. Fraunhofer ITWM. *MAVI – Modular Algorithms for Volume Images*, 2005.
34. Voronoi, G. Nouvelles applications des parametres continus à la théorie des forms quadratiques. *J. Reine. Angew. Math.* **1908**, *133*, 97–198.
35. Kharaghani, A.; Metzger, T.; Tsotsas, E. An irregular pore network model for convective drying and resulting damage of particle aggregates. *Chemical Engineering Science* **2012**, *75*, 267–278.
36. Jerauld, G.R.; Salter, S.J. The effect of pore-structure on hysteresis in relative permeability and capillary pressure: Pore level modeling. *Transport in Porous Media* **1990**, *5*, 103–151.
37. Scheel, M.; Seemann, R.; Brinkmann, M.; Michiel, M. Di.; Sheppard, A.; Herminghaus, S. Liquid distribution and cohesion in wet granular assemblies beyond the capillary bridge regime. *Journal of Physics: Condensed Matter* **2008**, *20*, 494236–7.